

Numerical evaluation of the phase-field model for brittle fracture with emphasis on the length scale

Xue Zhang¹ · Chet Vignes¹ · Scott W. Sloan¹ · Daichao Sheng¹

Received: 5 August 2016 / Accepted: 2 January 2017
© Springer-Verlag Berlin Heidelberg 2017

Abstract The phase-field model has been attracting considerable attention due to its capability of capturing complex crack propagations without mesh dependence. However, its validation studies have primarily focused on the ability to predict reasonable, sharply defined crack paths. Very limited works have so far been contributed to estimate its accuracy in predicting force responses, which is majorly attributed to the difficulty in the determination of the length scale. Indeed, accurate crack path simulation can be achieved by setting the length scale to be sufficiently small, whereas a very small length scale may lead to unrealistic force-displacement responses and overestimate critical structural loads. This paper aims to provide a critical numerical investigation of the accuracy of phase-field modelling of brittle fracture with special emphasis on a possible formula for the length scale estimation. Phase-field simulations of a number of classical fracture experiments for brittle fracture in concretes are performed with simulated results compared with experimental data qualitatively and quantitatively to achieve this goal. Furthermore, discussions are conducted with the aim to provide guidelines for the application of the phase-field model.

Keywords Phase-field model · Validation · Crack propagation · Length scale · Brittle fracture

1 Introduction

Griffith's theory [1], which regards fracture as a competition between the surface energy for crack formation and the elastic energy stored in the bulk material, is a classical criterion for predicting quasi-static fracture of brittle materials. However, Griffith's theory only provides a crack initiation criterion for existing cracks; it fails to predict the nucleation of new cracks and the crack propagation direction. Consequently, a supplemental criterion, such as the principle of local symmetry or the principle of maximal energy release, must be adopted for crack propagation problems.

To tackle the directional limitation of Griffith's theory, Francfort and Marigo [2] proposed a variational theory of fracture. By employing Griffith's energy release rate concept, a variational fracture model emerges from the global minimisation of a Griffith-like energy functional (a sum of the stored elastic energy of a material body and the surface energy of a crack set) with respect to any admissible displacement field and discontinuous crack set. Comparing to the classical linear elastic fracture theory that two separate criteria are adopted for predicting crack initiation and the crack propagation direction, respectively, this variational model is capable of predicting both of these two without employing any *ad-hoc* criteria [2, 3]. Nevertheless, the direct numerical implementation of this variational model is a challenge [2]. Two major difficulties are: (1) the displacement field at crack sets is discontinuous; and (2) the optimal crack set for the energy functional is unknown. To address these difficulties, a regularised form of the variational model was proposed by Bourdin et al. [4]. The regularised model replaces the discrete crack set with a smeared crack via the introduction of a phase field describing the continuous transition between fully broken and intact material phases.

✉ Xue Zhang
xue.zhang@uon.edu.au

¹ ARC Centre of Excellence for Geotechnical Science and Engineering, The University of Newcastle, Callaghan, NSW 2308, Australia

The method of crack representation proposed by Bourdin et al. [4], termed the “phase-field model” of fracture, is a smeared/diffusive approach. Alternatives to smeared/diffusive approaches are discrete methods which attempt to describe the exact topology of a crack surface in either an explicit (e.g. finite element edges are potential crack surfaces [5–10]) or implicit (e.g. extended finite element method [11–15]) manner. Compared to discrete approaches, the phase-field method requires neither remeshing techniques to alleviate mesh dependence of crack paths nor shape function enrichment near crack tips. Truly, numerical implementation of the phase-field model can be achieved straightforwardly, in both two and three dimensions, using the classical multi-field finite element method without any modification of initial meshes or shape functions [16, 17]. Due to this feature, complex fracture simulations, for example multiple crack sets, crack branching, and coalescence, can be handled without computational difficulties in the phase-field modelling [18, 19]. This, in contrast, is a critical challenge for discrete approaches particularly in three dimensions.

Considerable efforts have been devoted to further developing the phase field model in the mechanics community. For computational purposes, both monolithic and staggered schemes have been proposed. Typical monolithic schemes are the multi-field finite element formula developed by Miehe et al. [16] and Kuhn et al. [20], and the Abaqus-based implementation by Msekh et al. [21]. On the contrary, staggered schemes [17, 22, 23] attempt to solve displacement and phase fields in an alternate manner. Noting that the variational principle for fracture [2] and its regularised approximation [4] cannot distinguish between fracture behaviour in tension and compression, tension-compression partition was performed by Amor et al. [24] and by Miehe et al. [16, 17], respectively. The basic idea is to express the total elastic energy as a sum of active and inactive energy parts. The active energy part contributes to the crack evolution, whereas the inactive energy part, stemming from compressive stress states, does not. Although these modified phase-field models produce more realistic crack phenomena in some cases, as indicated by Ambati et al. [25] there has been so far no evidence showing whether they approximate to any variational principle in the sense as Γ convergence as the one proposed by Bourdin et al. [4]. Ambati et al. [25] also showed that the tension-compression partition leads the momentum balance equations to being highly nonlinear which consequently increases the computational cost. Indeed, how to enhance computational efficiency is a critical topic for phase-field modelling because a very fine mesh has to be used for resolving high gradients of crack field at critical zones. For the sake of computational efficiency, Ambati et al. [25] proposed a hybrid formulation which retains the linearity of momentum balance equations without losing the ability in preventing cracks in compressive stress states. Schilling et al. [26]

advocated the utilisation of isogeometric collocation methods because of the reduction of algorithm operation times at the quadrature point level. Kuhn and Muller [27] reported that a coarser mesh can be used by employing exponential shape functions due to their ability in capturing the analytical stationary solution of the crack field. In addition, adaptive refinement mesh techniques are usually adopted for the sake of computational efficiency. To date, the phase-field model has been adopted for modelling a number of challenging problems, for example dynamic fracture [18, 28, 29], ductile fracture [30–33], cohesive fracture [34–36], fracture in rubbery polymers [37], thin shells [38], thin films [39–41], and saturated porous media [42], hydraulic fracture [43–45], among others.

Despite these contributions, few systematic validation studies have been conducted for the phase-field model. Simulated brittle fracture in an asymmetrically notched beam is compared with available experimental data in [16]. In [25], comparison between simulation results and experimental data from both the literature (for L-shaped panel tests and asymmetrically notched beam tests) and performed tests (on notched plate with holes) is conducted to validate a proposed hybrid formulation for brittle fracture. Crack initiation and propagation in plaster specimens were reproduced in [46]. Some classical brittle fracture experiments were reproduced by the phase-field model in [47]. Notably, most of these validations focus on the predicted crack paths rather than the force-displacement response. Indeed, the quantitative prediction of the load-displacement response in a crack propagation problem is formidable and with phase-field modelling relies not only on the precise estimation of the critical energy release rate through experimental tests, but also on the appropriate determination of the length scale [16]. It has been shown that accurate crack path simulation can be achieved by simply setting the length scale, often interpreted as an arbitrary regularization parameter in the variational formulation of the phase-field model, to be sufficiently small. However, despite producing accurate crack paths, a very small length scale may lead to unrealistic force-displacement responses and overestimate critical structural loads. To date, there has been no such an approach that is widely accepted for determining the length scale parameter for phase-field modelling. Recently, an attempt to tackle this issue was made in [19, 28, 48], where a formula, derived analytically from a simple one-dimensional crack problem, was proposed. In the formula, the length scale is treated as a material parameter linked to the Young’s modulus, tensile strength, and critical energy release rate of the material. It was pronounced that such a treatment of the length scale may address the competition between accurate crack paths and accurate force-displacement responses; nevertheless, a critical evaluation of the performance of the proposed formula in phase-field modelling is not yet available. In [47],

the force-displacement curve obtained from the phase-field modelling, using the length scale estimated through the fore-mentioned approach, agrees perfectly with experimental data about cracks in concrete. However, it is also remarkable that the simulated phase field is rather diffusive compared with the size of the specimen, implying that the formula utilised for length scale estimation ensures the accurate prediction of force responses regardless whether the condition $l_0 \rightarrow 0$ is satisfied. This implication is in contrary to the convergence criterion of the regularised variational principle - the foundation of the phase-field mode, and thus demands further studies. Additionally, the proposed formula for the length scale estimation is derived based on the assumption of a constant phase field, whereas the tensile strength parameter needed in the formula is calibrated from the tensile test in which materials, for example concretes and rocks, experience cracks of strong discontinuity. Whether considerable errors will be induced by such an inconsistency also requires more validation studies. Last but not least, the performance of the formula for modelling mixed-mode cracks necessitates further testing since it is derived from the case of a pure tension crack.

In this paper, we attempt to provide a validation study of phase-field modelling of brittle fracture with particular emphasis on the length scale. More specifically, the length scale estimated through the formula proposed in [19, 28, 48] is set in the phase-field model and used to reproduce a number of classical fracture experimental tests on concretes with aims to highlight the effect of the length scale in accurate phase-field modelling, to evaluate this formula for length scale determination, and to systematically assess the capability of phase-field solutions for brittle fracture with respect to not only qualitatively correct crack paths but also quantitatively correct load-displacement curves.

The paper is organised as follows. Section 2 summarises the variational principle for brittle fracture. The governing equations for phase-field modelling of brittle fracture are then derived in Sect. 3. Section 4 describes the finite element discretisation and the utilised staggered scheme briefly, and Sect. 5 highlights the importance of the length scale in phase-field modelling through the theoretical analysis of a one-dimensional fracture problem, in which the formulation for the length scale estimation is also given. A number of classical experimental tests are simulated in Sect. 6 with qualitative and quantitative comparison between the simulated results and available experimental data being performed before conclusions are drawn in Sect. 7.

2 Variational principle for brittle fracture

Consider a brittle medium in the domain Ω bounded by its surface $\partial\Omega$ (Fig. 1a). Let $\mathbf{u}(\mathbf{x})$ be the displacement of a point

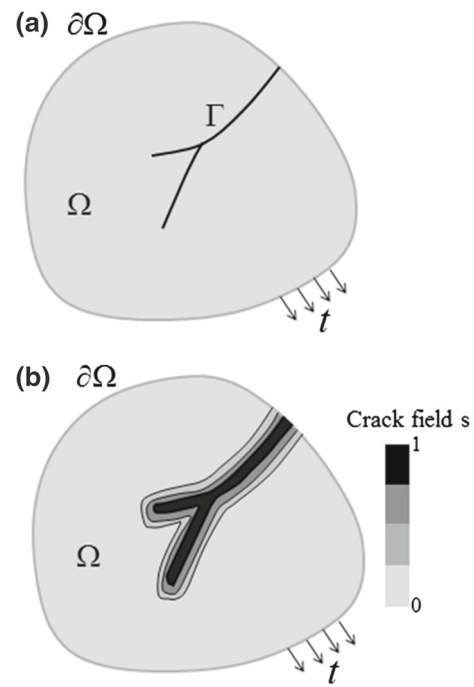


Fig. 1 **a** Schematic illustration of a body with cracks. **b** Representation of discrete cracks by phase field, s

\mathbf{x} . The infinitesimal strain at the point can then be denoted by

$$\boldsymbol{\varepsilon} = \nabla \mathbf{u} \quad (1)$$

with

$$\nabla = \begin{bmatrix} \frac{\partial}{\partial x} & 0 \\ 0 & \frac{\partial}{\partial y} \\ \frac{\partial}{\partial y} & \frac{\partial}{\partial x} \end{bmatrix} \quad (2)$$

being the linear gradient operator. Assume isotropic linear elasticity. Then, the elastic energy density of the material is

$$\psi = \frac{1}{2} \boldsymbol{\varepsilon}^T \mathbf{D} \boldsymbol{\varepsilon} \quad (3)$$

where \mathbf{D} is the elastic constitutive matrix. According to [2], the variational principle for brittle fracture is the minimization of the energy functional

$$\begin{aligned} \Pi(\mathbf{u}, \Gamma) = & \underbrace{\int_{\Omega \setminus \Gamma} \psi(\nabla \mathbf{u}) dV}_{\text{Bulk energy}} - \underbrace{\int_{\partial\Omega} \mathbf{t}^T \mathbf{u} dA}_{\text{External potential}} \\ & + \underbrace{\int_{\Gamma} G_c d\Gamma}_{\text{Surface energy}} \end{aligned} \quad (4)$$

with respect to the displacement field \mathbf{u} and the crack set Γ . Here, \mathbf{t} is the surface traction and G_c is the critical energy release rate (e.g. the energy required to create a unit area of new crack). It has been shown that this variational model is capable of predicting both crack initiation and propagation [2].

3 Phase-field model

The solutions to the variational model comprise a crack set Γ and an admissible displacement field \mathbf{u} . To circumvent numerical difficulties originating from discontinuities in the displacement field at the crack set, the discrete crack set Γ is smeared through the introduction of a phase field $s(\mathbf{x})$ (Fig. 1b). The phase field is a scalar between 0 and 1 representing the degree of material damage.

3.1 Regularised formulation

The regularised form of the variational principle for brittle fracture can be derived following [16]. Figure 2a shows an axial bar of infinite length with a cross-section Γ . The sharp crack topology is defined by the phase-field parameter with

$$s(x) = \begin{cases} 1, & \text{for cracked material} \\ 0, & \text{for intact material} \end{cases} \quad (5)$$

Assume that there exists a crack at the axial position $x = 0$, where Γ then denotes a crack surface. This crack can be approximated via a standard exponential function

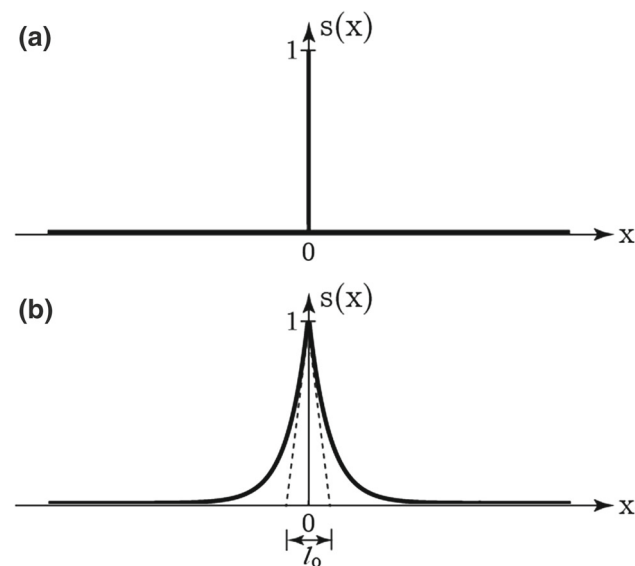


Fig. 2 **a** Sharp crack topology and **b** smeared crack representation for an infinite bar with a crack at $x = 0$

$$s(x) = e^{-|x|/2l_0} \quad (6)$$

where l_0 is a material length scale (Fig. 2b) [16]. This exponential function is a solution to the ordinary differential equation

$$-s''(x) + \frac{1}{4l_0^2}s(x) = 0 \quad (7)$$

with boundary conditions:

$$s(0) = 1 \text{ and } s(\pm\infty) = 0 \quad (8)$$

At this stage, construct the functional, $I(s) = \int_{-\infty}^{+\infty} \frac{1}{4}[s^2 + 4l_0^2 s'^2]dV$, which is the weak form of Eq. (7). Observing that $I(e^{-|x|/2l_0}) = l_0\Gamma$, introduce an alternative functional

$$\Gamma_l = \int_{-\infty}^{+\infty} \frac{1}{4l_0}[s^2 + 4l_0^2 s'^2]dV \quad (9)$$

whose minimisation also gives the regularised crack topology (6). In multi-dimensional cases, the corresponding functional can be expressed, using standard tensor notations, as

$$\Gamma_l = \int_{-\infty}^{+\infty} \frac{1}{4l_0} [s^2 + 4l_0^2 s_{,i} s_{,i}] dV \quad (10)$$

Using (10), the last surface term in energy functional (4) can now be approximated by

$$\int_{\Gamma} G_c dA \approx \int_{-\infty}^{+\infty} \frac{G_c}{4l_0} [s^2 + 4l_0^2 s_{,i} s_{,i}] dV \quad (11)$$

Due to the introduction of the phase field, a degradation function $g(s)$ must be introduced to reduce material stiffness after damage. Adopting a quadratic function $g(s) = (1 - s)^2$ and using Eq. (11), the energy functional (4) can be approximated as

$$\begin{aligned} \tilde{\Pi}(\mathbf{u}, s) = & \int_{\Omega} (1 - s)^2 \psi(\nabla \mathbf{u}) dV - \int_{\partial\Omega} \mathbf{t}^T \mathbf{u} dA \\ & + \int_{\Omega} \frac{G_c}{4l_0} [s^2 + 4l_0^2 s_{,i} s_{,i}] dV \end{aligned} \quad (12)$$

For $l_0 \rightarrow 0$, the regularised functional $\tilde{\Pi}$ from Eq. (12) reduces to the functional Π in Eq. (4) [49].

3.2 Governing equations

The governing equations for brittle fracture associated with the regularised variational model can be derived through variation of the functional (12) with respect to the displacement field, \mathbf{u} , and the crack field, s :

$$\begin{aligned} \delta \tilde{\Pi} = & \int_{\Omega} \sigma_{ij} \delta u_{i,j} d\Omega - \int_{\Omega} b_i \delta u_i dV - \int_{\partial\Omega} t_i \delta u_i d\Gamma \\ & - \int_{\Omega} 2(1-s)\psi \delta s d\Omega \\ & + \int_{\Omega} G_c \left(\frac{s}{2l_0} \delta s + 2l_0 s_{,i} \delta s_{,i} \right) d\Omega, \end{aligned} \quad (13)$$

where the body force, b_i , is also considered, and the stress σ_{ij} , is defined as

$$\sigma_{ij} = (1-s)^2 \frac{\partial \psi}{\partial \varepsilon_{ij}}. \quad (14)$$

Integrating the first and last terms by part, Eq. (13) reads

$$\begin{aligned} \delta \tilde{\Pi}(\mathbf{u}, s) = & \int_{\partial\Omega} (\sigma_{ij} n_j - t_i) \delta u_i dA - \int_{\Omega} (\sigma_{ij,j} + b_i) \delta u_i dV \\ & + \int_{\Omega} \left[-2(1-s)\psi + \frac{G_c}{2l_0} s - 2G_c l_0 s_{,ii} \right] \delta s d\Omega \\ & + G_c \int_{\partial\Omega} 2l_0 s_{,i} n_i \delta s dA \end{aligned} \quad (15)$$

As $\delta \tilde{\Pi}(\mathbf{u}, s) = 0$ must hold for all admissible displacement and phase fields, Eq. (15) yields the differential equations

$$\sigma_{ij,j} + b_i = 0 \text{ in } \Omega \quad (16)$$

$$(1-s)\psi - \frac{G_c}{4l_0} s + G_c l_0 s_{,ii} = 0 \text{ in } \Omega \quad (17)$$

and Neumann boundary conditions

$$\sigma_{ij} n_j = \bar{t}_i \text{ on } \partial\Omega_t \quad (18)$$

$$s_{,i} n_i = 0 \text{ on } \partial\Omega_{s'} \quad (19)$$

To prevent crack recovery, Eq. (17) is rewritten as

$$(1-s)\mathcal{H} - \frac{G_c}{4l_0} s + G_c l_0 s_{,ii} = 0 \text{ in } \Omega \quad (20)$$

where

$$\mathcal{H} = \max \psi \quad (21)$$

is the maximum reference energy—a history-field variable parameter [17]. In summary, the governing equations for phase-field modelling are:

$$\left. \begin{aligned} \sigma_{ij,j} + b_i &= 0 \text{ in } \Omega \\ (1-s)\mathcal{H} - \frac{G_c}{4l_0} s + G_c l_0 s_{,ii} &= 0 \text{ in } \Omega \\ u_i &= \bar{u}_i \text{ on } \partial\Omega_u, \quad s = \bar{s} \text{ on } \partial\Omega_s \\ \sigma_{ij} n_j &= \bar{t}_i \text{ on } \partial\Omega_t, \quad s_{,i} n_i = 0 \text{ on } \partial\Omega_{s'} \end{aligned} \right\} \quad (22)$$

The third set of the above equations are Dirichlet boundary conditions. The partitions of the boundary satisfy the

constraints that $\partial\Omega_t \cup \partial\Omega_u = \partial\Omega_s \cup \partial\Omega_{s'} = \partial\Omega$ and $\partial\Omega_t \cap \partial\Omega_u = \partial\Omega_s \cap \partial\Omega_{s'} = \emptyset$, where \emptyset is a null set.

Notably, crack evolution Eq. (20) does not distinguish between fracture behaviour in tension and compression when adopting the definition of \mathcal{H} shown in Eq. (21), and may produce unrealistic crack patterns in compression as reported in [4]. According to [17], this limitation can be tackled by first expressing the elastic energy density ψ as the sum of a tension part ψ^+ and a compression part ψ^- , using the definitions:

$$\psi^{\pm} = \lambda \langle \text{tr}[\boldsymbol{\varepsilon}] \rangle_{\pm}^2 + \mu \text{tr}[\langle \boldsymbol{\varepsilon} \rangle_{\pm}^2] \quad (23)$$

where the spectral decomposition of the strain tensor $\boldsymbol{\varepsilon} = \sum_{I=1}^3 \varepsilon_I \mathbf{n}_I \otimes \mathbf{n}_I$ is employed (ε_I and \mathbf{n}_I are the principal strains and principal strain directions) and the bracket operator is defined as $\langle x \rangle_+ = (x + |x|)/2$. λ and μ are the Lamé constant and shear modulus, respectively. Here, only the positive part ψ^+ contributes to the crack evolution [17], namely

$$\mathcal{H} = \max \psi^+ \quad (24)$$

which is the maximum positive reference energy. An alternative decomposition of ψ to (23) was proposed by Amor et al. [24]. The definition of the history variable \mathcal{H} in Eq. (24), enables the crack evolution equation to distinguish between fracture behaviour in compression and tension and has been widely used; however, it is also notable that strict convergence proofs of the phase-field model with Eq. (24) to any variational formula are not yet available.

4 Finite element discretisation

The staggered solution scheme for the governing equations is utilised in this paper [17, 25]. In the scheme, the governing equations are divided into two sets, namely,

$$\begin{aligned} \text{set 1 } & \begin{cases} \sigma_{ij,j} + b_i = 0 & \text{in } \Omega \\ u_i = \bar{u}_i & \text{on } \partial\Omega_u \\ \sigma_{ij} n_j = \bar{t}_i & \text{on } \partial\Omega_t \end{cases} \quad \text{and} \\ \text{set 2 } & \begin{cases} (1-s)\mathcal{H} - \frac{G_c}{4l_0} s + G_c l_0 s_{,ii} = 0 & \text{in } \Omega \\ s = \bar{s} & \text{on } \partial\Omega_s \\ s_{,i} n_i = 0 & \text{on } \partial\Omega_{s'} \end{cases} \end{aligned} \quad (25)$$

In a typical incremental step, the first set of equations is solved for the stress field with the phase field fixed. Next, the phase field is resolved based on the second set of equations using the updated displacement field. Iterations between these two steps are continued until the convergence criterion is fulfilled.

The governing equations are solved numerically using the finite element method. Approximations to the displacement field and phase field are

$$\mathbf{u}(\mathbf{x}) \approx \mathbf{N}_u \hat{\mathbf{u}}, \quad s(\mathbf{x}) \approx \mathbf{N}_s \hat{\mathbf{s}} \quad (26)$$

where \mathbf{N}_u and \mathbf{N}_s are matrices consisting of corresponding shape functions, and $\hat{\mathbf{u}}$ and $\hat{\mathbf{s}}$ are vectors of displacements and phase fields at element nodes. Using the approximations (Eq. 26), the discretised weak form of the governing equations for brittle fracture can be expressed as

$$\int_{\Omega} \mathbf{B}_u^T \tilde{\mathbf{D}} \mathbf{B}_u dV \hat{\mathbf{u}} = \int_{\Omega} \mathbf{N}_u^T \mathbf{b} dV + \int_{\partial\Omega} \mathbf{N}_u^T \mathbf{t} dA \quad (27)$$

$$\left(\int_{\Omega} \mathbf{N}_s^T \left(\mathcal{H} + \frac{G_c}{4l_0} \right) \mathbf{N}_s dV + \int_{\Omega} \mathbf{B}_s^T G_c l_0 \mathbf{B}_s dV \right) \hat{\mathbf{s}} = \int_{\Omega} \mathbf{N}_s^T \mathcal{H} dV \quad (28)$$

Here $\tilde{\mathbf{D}}$ is the degraded constitutive matrix, and matrices \mathbf{B}_u and \mathbf{B}_s in Eqs. (27) and (28) take the form of

$$\mathbf{B}_u = \begin{bmatrix} \frac{\partial N_1^u}{\partial x} & 0 & \dots & \frac{\partial N_l^u}{\partial x} & 0 \\ 0 & \frac{\partial N_1^u}{\partial y} & \dots & 0 & \frac{\partial N_l^u}{\partial y} \\ \frac{\partial N_1^u}{\partial y} & \frac{\partial N_1^u}{\partial x} & \dots & \frac{\partial N_l^u}{\partial y} & \frac{\partial N_l^u}{\partial x} \end{bmatrix} \text{ and} \quad (29)$$

$$\mathbf{B}_s = \begin{bmatrix} \frac{\partial N_1^s}{\partial x} & \frac{\partial N_2^s}{\partial x} & \dots & \frac{\partial N_l^s}{\partial x} \\ \frac{\partial N_1^s}{\partial y} & \frac{\partial N_2^s}{\partial y} & \dots & \frac{\partial N_l^s}{\partial y} \end{bmatrix}$$

where N_i^u and N_i^s are shape functions for the displacement and phase fields, respectively, with i representing the number of element nodes.

5 Influence and determination of length scale

The length scale l_0 is an important parameter for the phase-field model. It has been proven that the regularized formulation (12) converges to the original variational formulation (4) when the length scale $l_0 \rightarrow 0$ [49]. This implies that numerically the length scale should be set as small as possible. However, the length scale is not only an arbitrarily small regularisation parameter and care must be exercised in its determination. Recently, a possible way to determine the length scale parameter was proposed in [19, 28, 48], which is summarised in the following.

Consider a one-dimensional homogeneous, weightless bar with a length L subject to a displacement \bar{u} at the right end and fixed at the left end (Fig. 3). Young's modulus of the material is denoted by E . In this case, the linear momentum balance and crack evolution equations can be written as



Fig. 3 A homogeneous bar subject to a displacement load

$$\frac{d\sigma_x}{dx} = 0 \quad \text{in } \Omega \quad (30)$$

$$(1-s)\psi - \frac{G_c}{4l_0}s + G_c l_0 \frac{d^2 s}{dx^2} = 0 \quad \text{in } \Omega \quad (31)$$

with boundary conditions

$$u_x(x=0) = 0 \quad \text{and} \quad u_x(x=L) = \bar{u} \quad (32)$$

$$\frac{ds}{dx} \Big|_{x=0} = 0 \quad \text{and} \quad \frac{ds}{dx} \Big|_{x=L} = 0 \quad (33)$$

where $u_x(x)$ is the displacement of the point at x . Note that the bar is homogeneous, so Eqs. (30) and (33) are fulfilled naturally as the strain, stress and crack fields across the bar are uniform. The strain $\varepsilon_x(x)$ is expressed as

$$\varepsilon_x = \frac{\bar{u}}{L} \quad (34)$$

which yields the elastic energy density

$$\psi = \frac{1}{2} \frac{E \bar{u}^2}{L^2} \quad (35)$$

and the stress

$$\sigma_x = (1-s)^2 \frac{E \bar{u}}{L} \quad (36)$$

Now, the homogeneous crack field can be solved by substituting Eq. (36) into Eq. (31) giving

$$s = \frac{2El_0 \bar{u}^2}{2El_0 \bar{u}^2 + G_c L^2} \quad (37)$$

Substituting Eq. (37) into Eq. (36) leads to the stress

$$\sigma_x = \frac{G_c^2 L^3 E \bar{u}}{(2El_0 \bar{u}^2 + G_c L^2)^2} \quad (38)$$

By focusing on the optimization condition $\frac{d\sigma_x}{d\bar{u}} = 0$, the displacement at the stationary point is found to be

$$\bar{u}^* = \sqrt{\frac{G_c L^2}{6El_0}} \quad (39)$$

and, consequently, the maximum critical stress that the bar can sustain is

$$\sigma_{cr} = \frac{9}{16} \sqrt{\frac{EG_c}{6l_0}} \quad (40)$$

As indicated in [28], although the length scale l_0 has to be sufficiently small to ensure the convergence of the regularised variational model to the original model, an infinitesimal length scale will produce an infinitely large critical stress which is physically unrealistic. Thus, the length scale cannot be regarded as an arbitrarily small parameter in the phase-field model. Rather, it should be considered a material parameter determined from Eq. (40) as

$$l_0 = \frac{27EG_c}{512\sigma_{cr}^2} \quad (41)$$

Given that the Young's modulus and the critical energy release rate can be determined through standard experimental tests, the length scale parameter can be evaluated through the above equation after the tensile strength σ_{cr} is obtained through the standard tensile test. Notably, Eq. (41) is for estimating the length scale parameter of brittle materials. The estimation formula for phase-field modelling of more complex fracture, for example ductile fracture or fracture in saturated porous media, should be different because the corresponding governing equations differ [30, 42, 43]. However, it can also be derived based on the one-dimensional crack following the above procedure. It is remarkable that, although above formula for determining the length scale parameter is advocated in [19, 28, 48], its performance in the phase-field modeling requires further evaluated against experimental results.

6 Numerical experiments

In this section, a specimen under tension is analysed first to highlight the importance of the length scale. Next, a number of classical fracture tests are simulated for performance evaluation. In all simulations, six-node triangular elements are used and the length scale is considered a material parameter that is evaluated using Eq. (41). Since the stress state of the specimens is mainly tension for most of the selected experimental tests, the tension-compression decomposition is not needed and the definition of the history variable \mathcal{H} in (21) is used. An exception is the Nooru-Mohamad test for mixed-mode cracks, where the stress state is much more complex.

6.1 A specimen under tension

To highlight the effect of the length scale parameter in the phase-field modelling, we here consider a specimen subject to a displacement u as shown in Fig. 4. The material parameters of the specimen are as follows: Young's modulus $E = 1 \times 10^6$ Pa, Poisson's ratio $\nu = 0.49$, and the critical energy release rate, $G_c = 100$ N/m. The displacement imposed on the specimen is 0.015 m. The bar is discretised using 10,800 uniform elements with edge length $h = 0.01$ m. Three values of the length scale ($l_0 = 0.025$, 0.05, and 0.075 m) are selected for the simulations, and a total of 100 increment steps are utilised to impose the displacement gradually.

Figure 5 illustrates the predicted distribution of the crack phase field s along the line $y = 0$ at the onset of cracking. For all cases, a smooth transition of the phase field from the middle of the bar where the material is cracked ($s = 1$) towards the two ends is observed. However, the distributions differ in the width of the damage zone where the phase field s is non-zero. A larger length scale leads to a degradation of material strength in a wider band. This coincides with the definition of the length scale depicted in Fig. 2b. Notably, for $l_0 = 0.075$ m, the phase field on the two ends is even greater than zero. The force-displacement curves are plotted in Fig. 6.

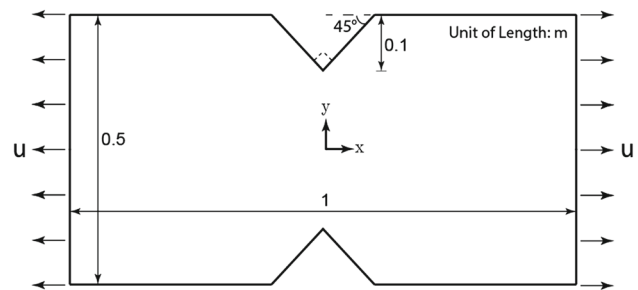


Fig. 4 The geometry of a specimen subject to tension

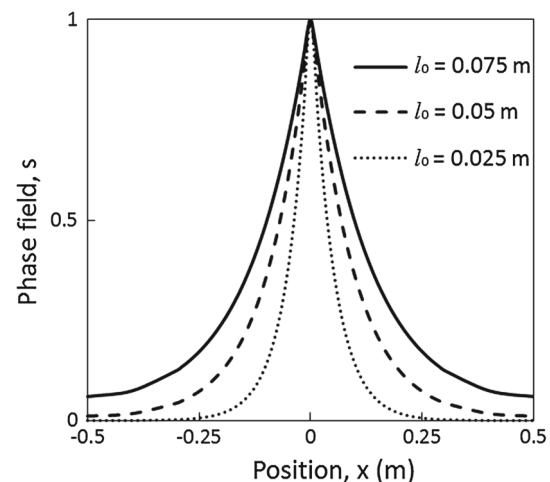


Fig. 5 Phase field distribution along the plane $y = 0$

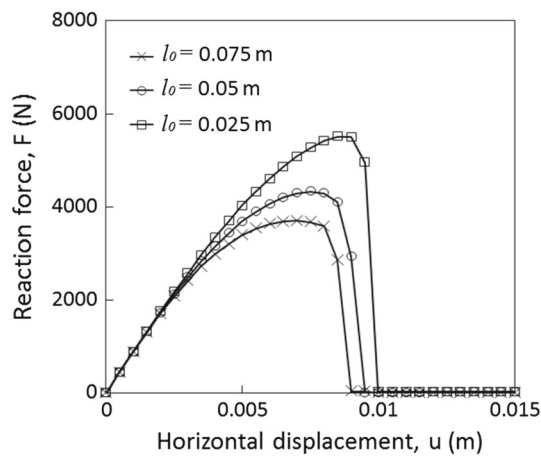


Fig. 6 Load-displacement curves from the phase-field modelling using different length scale

For all cases the reaction force rises steadily to a maximum value and then drops sharply to zero at cracking. However, the maximum force increases with decreasing length scale.

Additionally, the convergence of the applied phase-field model with respect to the utilised mesh size is tested. To this end, the above problem with the length scale parameter $l_0 = 0.05$ m is re-analysed using different mesh sizes. Figure 7a shows that a converged solution of the critical force response can be obtained for $h/l_0 \leq 0.5$. Furthermore, the effect of the adopted increment step on the predicted critical force is also investigated. The results obtained from both the staggered schemes with and without iterations using different time steps are illustrated (Fig. 7b). For the concerned problem, nearly 1000 time steps have to be used to maintain the simulation accuracy when no iteration is performed within staggered steps. In contrast, a converged solution can be obtained using just a total of 100 time steps when performing iterations in the staggered step. To maintain the simulation accuracy, small step increments are utilised with fine meshes assigned to critical zones in the following studies.

6.2 Three-point bending test

The three-point bending test of a notched plain concrete beam performed by Perdikaris and Romeo [50] is simulated in this section. The geometry and the experimental setup are illustrated in Fig. 8 (according to the test C2-D1-S3-R2 in [50]). Young's modulus is $E = 48.3$ GPa as reported in [50], and Poisson's ratio is assumed to be $\nu = 0.2$. In [50], the size effect on the fracture energy of concrete was investigated through evaluating the critical energy release rate using four different models. Here the value estimated based on Bazant's "size effect" model is used, namely, $G_c = 45.1$ N/m. As shown in [50], this model tackles the issue of size dependency in the sense of providing a unique G_c for specimens

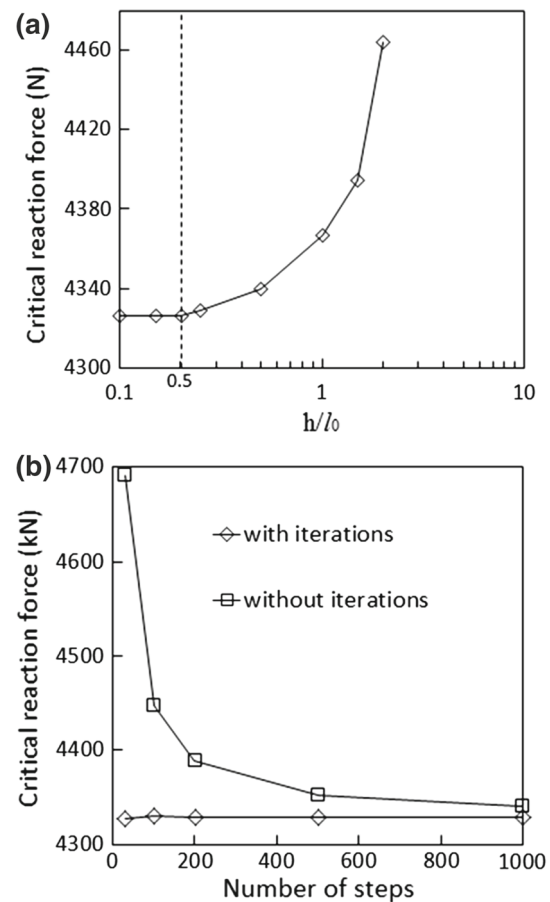


Fig. 7 Convergence of the phase-field modelling with respect to **a** the mesh size, and **b** the number of increment steps

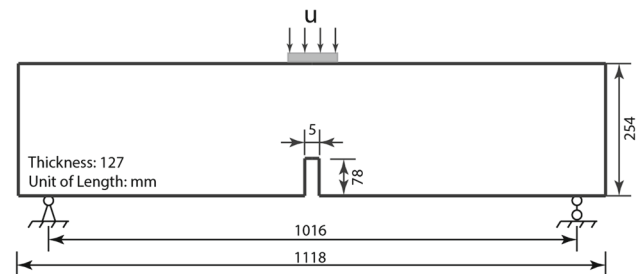


Fig. 8 Schematic illustration of the three-point bending test of a notched beam

with different sizes. As no tensile strength is provided in [50], assume $\sigma_{cr} = 3.33$ MPa which is a typical value for plain concretes [51]. The length scale l_0 calculated using Eq. (41) is $l_0 = 10.4$ mm.

The problem is regarded as plane-stress, and a total of 41,919 six-node triangular elements are utilised to discretize the domain. For the sake of computational efficiency, fine meshes with edge size $h = \frac{1}{10}l_0$ are assigned to the expected crack propagation zones and coarse meshes are adopted elsewhere. Simulations are performed under displacement

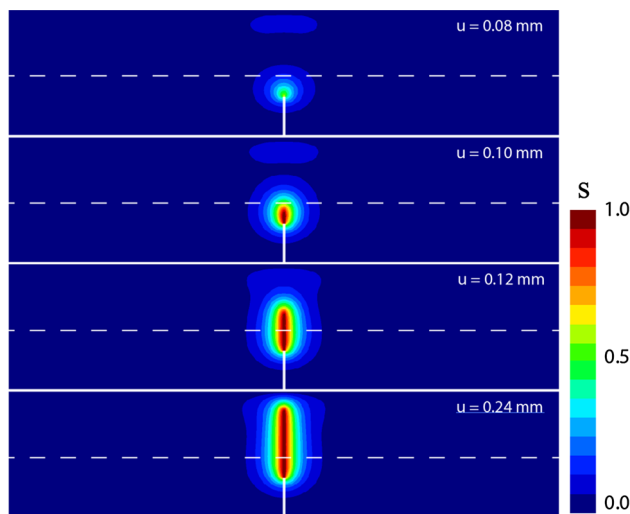


Fig. 9 Crack evolution in the beam subject to the displacement. The white dash line represent the plane $y = 120$ mm

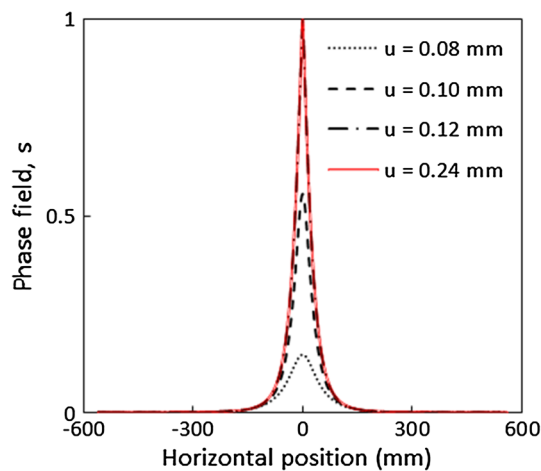


Fig. 10 The distribution of the phase field at the plane $y = 120$ mm

control with an incremental displacement $\Delta u = 0.01$ mm at each step.

Figure 9 illustrates the crack evolution process predicted from the phase-field model. The crack initiates from the notch tip and propagates towards the top surface of the beam. The distribution of the phase field, s , at the plane $y = 120$ mm (Fig. 9) is depicted in Fig. 10. As expected, the maximum values of the crack field at different loading stages are always located at the position $x = 0$ and the crack field decreases steadily to zero as $|x|$ increases. An increase in the imposed displacement increases the magnitude of the non-zero phase field but does not lead to a change in the width. When the phase-field reaches 1 (representing fully damaged), the distribution of the phase field remains unaltered regardless of further increases in the displacement; the distributions of the crack field at $u = 0.12$ mm and $u = 0.24$ mm are equal.

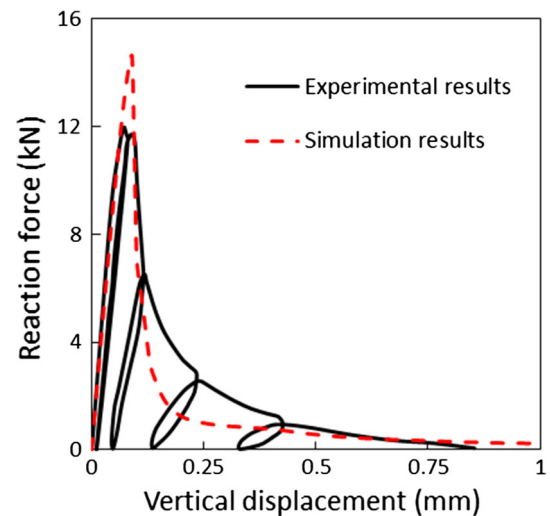


Fig. 11 Load-displacement curves for the three-point bending test

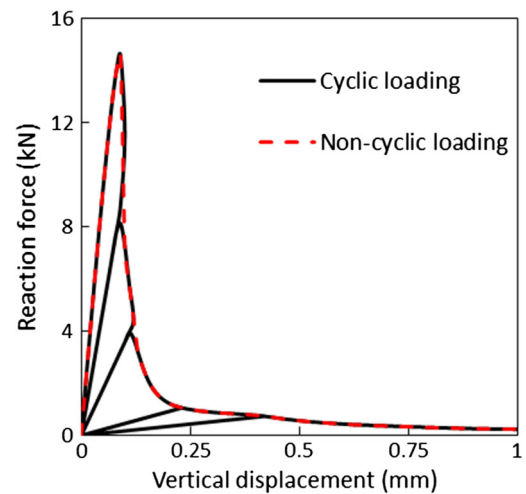


Fig. 12 Simulated load-displacement curves for the three-point bending test under both non-cyclic and cyclic loadings

Figure 11 compares the load-displacement response from this study to the experimental data. In the simulation, the beam is subject to non-cyclic loading. The maximum force that the beam can sustain from the simulation is 14.5 kN which is 20.8% higher than the experimental data (12.0 kN). The simulated force also drops much faster than the experimental data after reaching the bearing capacity. These deviations on one aspect stem from the fact that a linear fracture model is used in the simulation whereas the real fracture is nonlinear; the model neglects any plastic deformation. It can be clarified by examining the load-displacement curves from both cyclic and non-cyclic loadings. In Fig. 12, no residual deformation is maintained in the simulation after unloading which is typical when using phase-field models for brittle fracture [16, 17, 25], whereas residual deformation is observed at the end of each unloading in the experimental

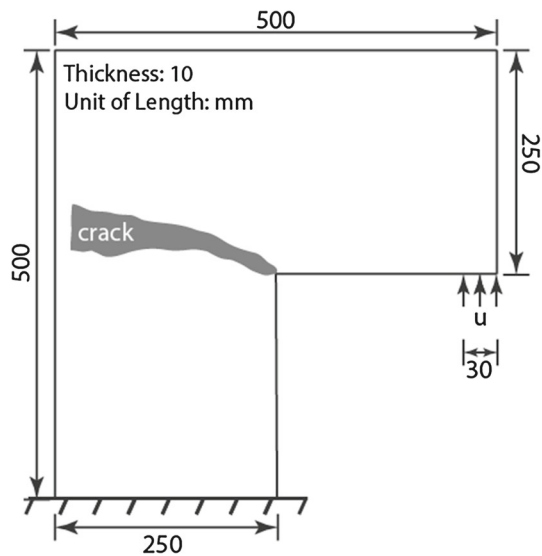


Fig. 13 Schematic illustration of the fracture test on a L-shaped concrete specimen

test (Fig. 11). On the other aspect, the deviation in terms of the critical force results from the inconsistency in the crack modes. The formula for estimating the length scale parameter is derived on the assumption of a constant phase field, whereas the tensile strength utilized in the formula is calibrated from the tensile test where the crack mode is not so. Despite these differences, the results from the phase-field modelling are overall comparable to the experimental data and much more accurate than results for simulations with smaller, arbitrarily selected length scales.

Remarkably, the calibration of the critical energy release rate, G_c , has long been recognized as a challenge. The fracture energy values determined from a series of three-point bending tests on concretes may differ considerably [50], and such an uncertainty is more obvious for composite materials [52]. To evaluate the sensitivity of predicted critical force response with respect to G_c , the three-point bending test is simulated with the critical energy release rate being $0.5G_c$ and $1.5G_c$ ($\pm 50\%$ error rate), respectively. For the case of $0.5G_c$, the predicted critical force is 11.07 kN, which is 24% lower than 14.5 kN, while the fracture energy of $1.5G_c$ results in a critical force at 17.98 kN which is 23.4% higher.

6.3 Fracture test on a L-shaped concrete specimen

The third example considered is the L-shaped experiment reported in [53], the setup of which is depicted in Fig. 13. The concrete specimen is fixed to a foundation at the bottom and loaded by a vertical displacement at the right. The material parameters from [53] are: $E = 25.85$ GPa, $\nu = 0.18$, and $G_c = 95$ N/m. The tensile strength σ_{cr} is assumed to be 2.7 MPa according to [47] where the problem was reproduced

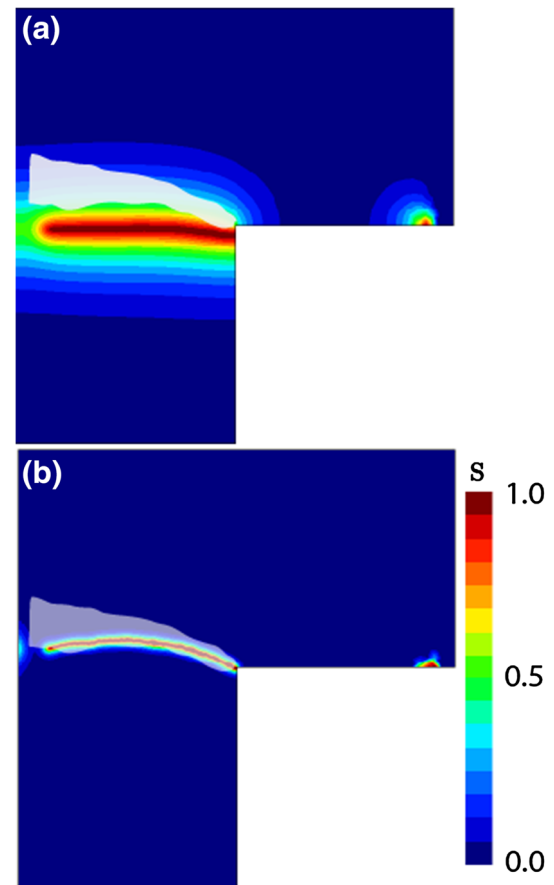


Fig. 14 Crack paths from the phase-field modelling and the experimental test

numerically using the phase-field model. Using Eq. (41), the length scale is evaluated to be $l_0 = 17.76$ mm. The simulation is led with the step increment $\Delta u = 2 \times 10^{-3}$ mm. The computational domain is discretised using a total of 11,293 elements with fine meshes ($h = \frac{1}{10}l_0$) assigned to the critical zone.

Figure 14a illustrates the crack path obtained from the phase-field modelling and superimposes the range of experimentally obtained crack paths (shaded region). For $l_0 = 17.76$ mm, a diffusive crack path is obtained due to the relatively large length scale (compared to the size of the specimen). Additionally, the crack path from the simulation is located below the path observed in the real test. The corresponding load-displacement curves are shown in Fig. 15; the shaded region is again the experimental data range. The reaction force from the simulation ($l_0 = 17.76$ mm) increases steadily to a maximum value and then drops sharply. The predicted maximum reaction force is nearly 50% higher than the experimental force. To further investigate the effect of the length scale, a second simulation is performed with a smaller length scale ($l_0 = 2.0$ mm). Although the maximum force obtained by using $l_0 = 2.0$ mm is even much higher

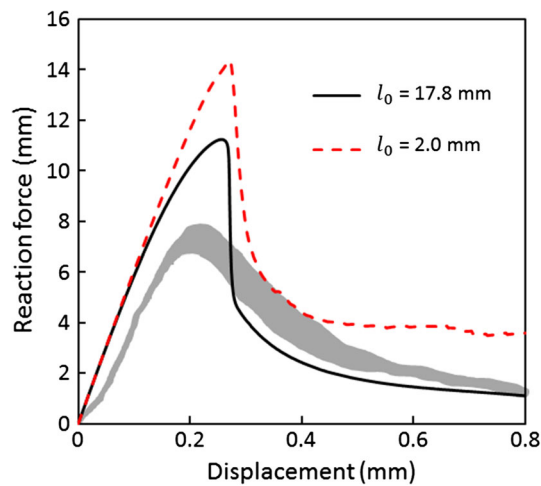


Fig. 15 Load-displacement curves from the phase-field modelling and the experimental test

(Fig. 15), the predicted crack path agrees well with the experimental data (Fig. 14b). Notably, the concerned problem has also been studied in [47], where the length scale parameter was considered a material parameter and a perfect agreement in force-displacement curves is obtained. The simulated results in [47] differ from the results presented here because a different regularised variational formula was adopted in [47]. However, such an agreement cannot give credits to the utilised model because the estimated l_0 is considerably large compared with the size of the specimen and a rather diffusive crack was obtained from the modelling. In such a case the convergence of the regularised variational model to the original one cannot be guaranteed. It is true that the ratio of the length scale l_0 to the specimen size plays an important role in phase-field modelling which will be investigated quantitatively by reproducing a series of fracture tests on specimens with different sizes in the section followed.

6.4 Wedge splitting test

To further investigate the effect of the ratio of the length scale l_0 and the specimen geometry on the phase-field modelling, the wedge splitting test conducted by Trunk [54] is considered. The schematic diagram of the wedge splitting specimen is shown in Fig. 16. Here focus is on the fracture tests on a dam concrete, denoted by CP250 in [54]. A series of tests (see Table 1) were conducted on specimens with different sizes. From [54], the material parameters are: $E = 28.3$ GPa, $\sigma_{cr} = 1.59$ MPa, and $G_c = 196.1$ N/m. In the simulation, Poisson's ratio is assumed to be $\nu = 0.2$. The values of tensile strength and the critical energy release rate utilised here were obtained from direct tension tests [54]. In the present context, the problem is considered to be plane-stress and the simulation proceeds under displace-

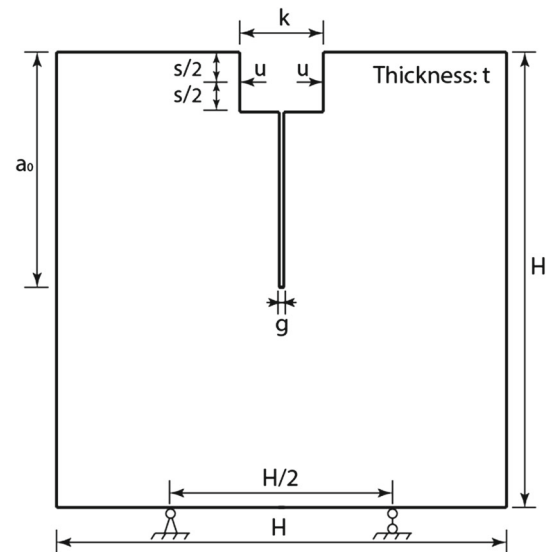


Fig. 16 The setup of wedge splitting tests

Table 1 Material parameters for the simulation of wedge splitting tests

Series	H	t	s	k	a_0	g
S1	400	400	100	100	175	5
S2	800	400	100	100	375	5
S3	1600	400	100	100	775	5
S4	3200	400	100	100	1575	5

ment control with step increment $\Delta u = 0.01$ mm. At the critical area a fine mesh is used with mesh size $h = \frac{1}{10}l_0$ (the length scale $l_0 \approx 115.7$ mm estimated using Eq. (41)) and a coarse mesh is employed elsewhere to reduce the computational cost.

Figure 17 illustrates the load-displacement curves for tests S1 and S4 (see also Table 1) obtained from phase-field modelling along with experimental data [54]. As expected, force response trends from the phase-field modelling coincide with the experimental data except for a sharper decline in the force after the maximum value is reached. Figure 17 also indicates the degree of variance of the estimated maximum force between these two tests. For test S4 (a large specimen, $H = 3200$ mm), the maximum force from this study is 149.5 kN which is 5.08% lower than the reported value (157.5 kN). In contrast, a nearly 100% gap between the maximum forces from the simulation and experimental test is observed for test S1 (a small specimen, $H = 400$ mm). This diversity results from the difference in the ratio l_0/H for the tests. It is reported in [4] that the regularised variational principle converges to the original when l_0 approaches zero. In other words, for this study the phase-field model is valid only when the length scale is much smaller than the geometry of specimens. For test S1, the ratio l_0/H is large (around 25.9%) leading to a

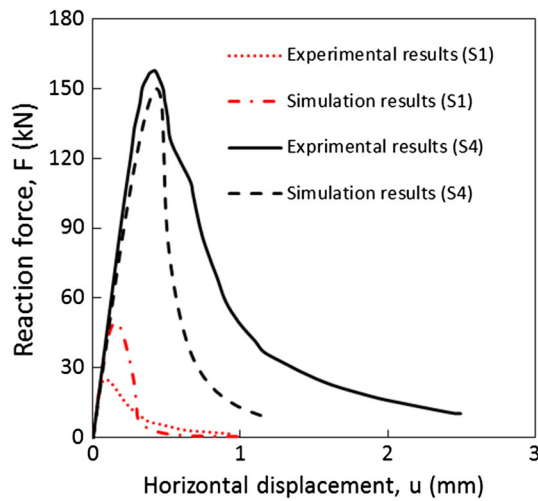


Fig. 17 Load-displacement curves for the tests on specimens with different sizes

rather diffusive crack field (Fig. 18a). As shown in Fig. 19, the minimum value of the field variable s (located at the lateral boundaries) along the plane $y = \frac{1}{4}H$ is nearly 0.5. Consequently, an apparent deviation of the simulated results from the experimental data is observed for test S1. In contrast, for test S4 the ratio l_0/H is relatively small (around 3.6%) and the width of the crack field is narrow compared to the size of the specimen (Fig. 18b); thus satisfactory agreement is obtained regarding the maximum reaction force. Further illustration of the l_0/H effect is obtained by considering the estimation error of the maximum force, $|F_{\max}^{\text{sim}} - F_{\max}^{\text{exp}}| / F_{\max}^{\text{exp}}$ (where F_{\max}^{sim} and F_{\max}^{exp} are the maximum reaction forces from this study and experimental tests, respectively) for all tests (S1 – S4). The simulated maximum reaction forces are much closer to the experimental data as the specimen size is increased (Fig. 20). For this geometry, the ratio l_0/H must be less than 4% to achieve under 10% error. These results show that, regardless whether the length scale is considered a material parameter, it has to be sufficiently small to predict accurate force responses in the phase-field modelling.

6.5 Nooru-Mohamad test

The last benchmark problem concerned is the mixed-mode fracture test performed by Nooru-Mohamad [51]. The schematic diagram of the problem is shown in Fig. 21a. A series of tests with different load paths have been performed to investigate the effect of shear force F_s on crack modes in [51]. In this section, focus is on the test under the load path 4b. The square size of the specimen is $H = 200$ mm and the thickness is 50 mm. First, a compressive shear load $F_s = 10$ kN is applied to the specimen. During this process, the top and bottom surfaces are fixed in the vertical direction. Next, a vertical displacement u_n is applied on top and bottom surfaces while

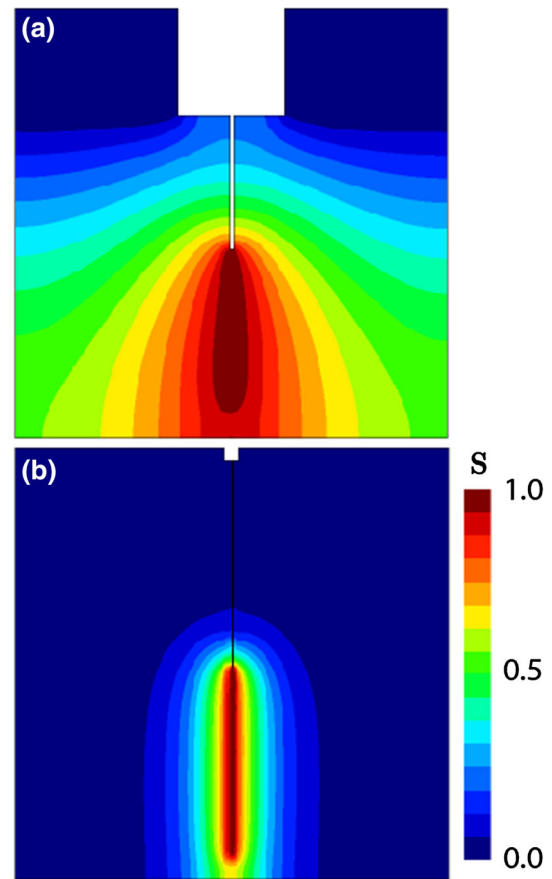


Fig. 18 The distribution of the phase field for a S1 test ($H = 400$ mm) and b S4 test ($H = 3200$ mm)

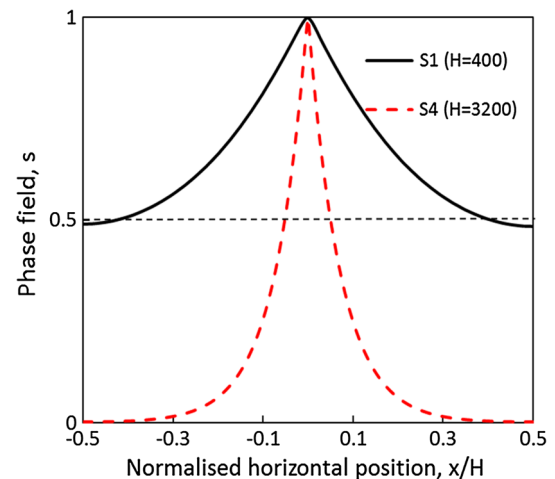


Fig. 19 The distribution of the phase field along the plane $y = \frac{1}{4}H$

keeping the lateral force F_s constant. In the simulation, the problem is considered as plane-stress and the material parameters quoted in [51] are used: $E = 30$ GPa, $\sigma_{cr} = 3.78$ MPa, and $G_c = 110$ N/m. Poisson's ratio is assumed to be $\nu = 0.2$. Accordingly, the length scale estimated using Eq. (41) is

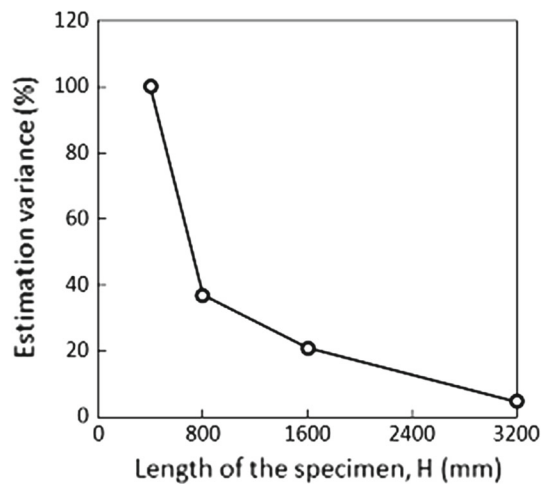


Fig. 20 Estimation variance of the bearing capacities versus the specimen size H

$l_0 = 12.18$ mm. The mesh size is relatively small ($h = \frac{1}{10}l_0$) at the expected crack propagation zone while a coarse mesh is used elsewhere. The displacement increment Δu_n at each time step is 1×10^{-4} mm.

The problem is first simulated using the phase-field model without the decomposition of elastic energy density. Figure 22a1–a3 illustrates the predicted process of crack propagation evolution from the phase-field modelling for length scale $l_0 = 12.18$ mm, where the normalised displacement is defined as $\delta_n = 2u_n/H$. Diffusive crack paths were obtained from the simulation which do not match those observed in the experimental test (Fig. 21b). This can be explained as follows. The convergence of the phase-field model to the variational model requires the length scale to be sufficiently small compared to the specimen as observed from Sect. 6.4. In this case, there are two cracks occurring in

the specimen and the vertical distance between these cracks is around 80 mm (Fig. 21b). The length scale leads to very diffusive cracks (Fig. 22a) which interact (Fig. 22b) and further contribute to the deviation of crack directions. Eventually, these two cracks coalesce and break the specimen horizontally (Fig. 22c).

It is expected that the predicted crack paths may be closer to the experimental data if the ratio l_0/H is reduced. Here, the specimen is enlarged to be 10 times ($H = 2000$ mm) the original size. The shear force F_s is scaled to 1000 kN such that the average normal pressure on the lateral surface, P_s , does not change. Figure 22b1–b3 illustrate the crack evolution processes. The left crack propagates obliquely towards the bottom surface while the right crack propagates towards the top surface. This matches the experimental observations (Fig. 21b). In spite of this agreement, crack coalescence occurs again. This is because a rather high compression stress state exists at the middle of the specimen, and the phase-field model without tension-compression decomposition cannot prevent crack evolution in compression.

To obtain the correct crack paths, the decomposition of the elastic energy density should be conducted and the definition of \mathcal{H} in (24), implying that only tensile component of energy contributes to crack evolution, has to be utilised. The crack evolution process predicted using this modified model is illustrated in Fig. 23. For $H = 200$ mm, again very diffusive cracks are obtained which coalesce due to interaction (Fig. 23a1–a3), which again emphasises the importance of the ratio between the length scale parameter and the specimen size. In contrast, the predicted crack paths for $H = 2000$ mm (Fig. 23b1–b3) coincide well with those observed in the experimental test.

The simulated reaction force for $H = 2000$ mm is compared with experimental data. Figure 24 shows the normalised aver-

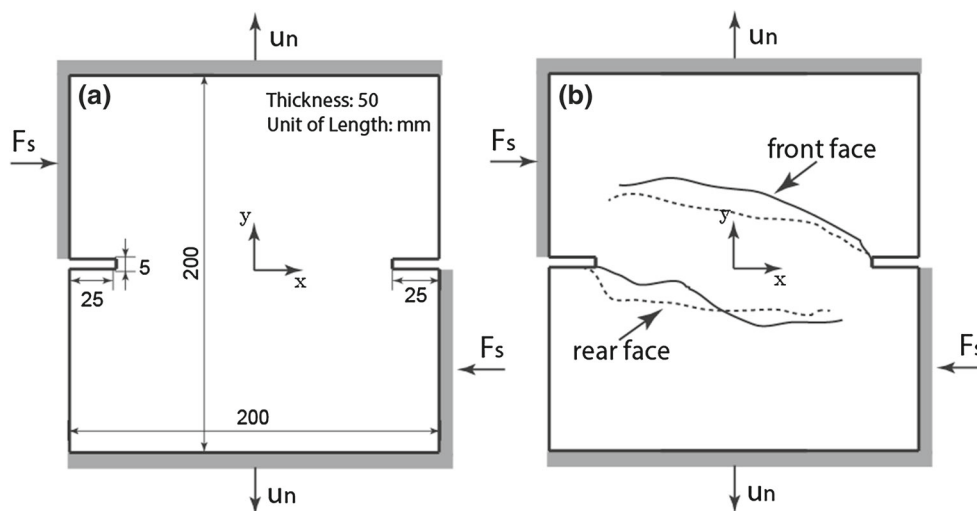


Fig. 21 **a** Schematic diagram of the tension shear test; and **b** crack paths from the experimental test

Fig. 22 Evolution of cracks for **a1** $H = 200$ mm, $\delta_n = 2.29 \times 10^{-4}$, **a2** $H = 200$ mm, $\delta_n = 2.3 \times 10^{-4}$, **a3** $H = 200$ mm, $\delta_n = 2.31 \times 10^{-4}$, **b1** $H = 2000$ mm, $\delta_n = 6.65 \times 10^{-5}$, **b2** $H = 2000$ mm, $\delta_n = 6.8 \times 10^{-5}$, and **b3** $H = 2000$ mm, $\delta_n = 7.15 \times 10^{-5}$

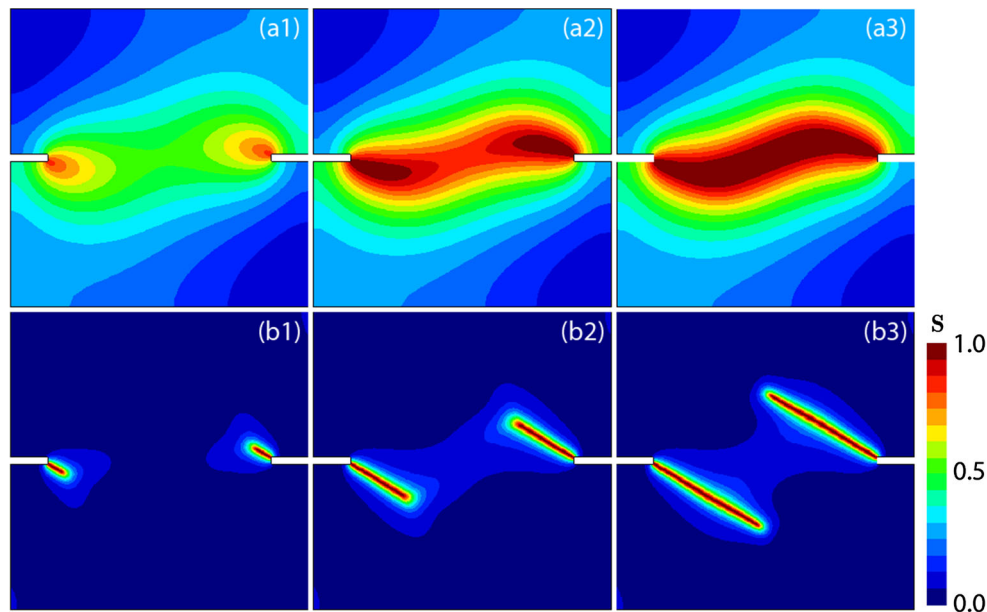
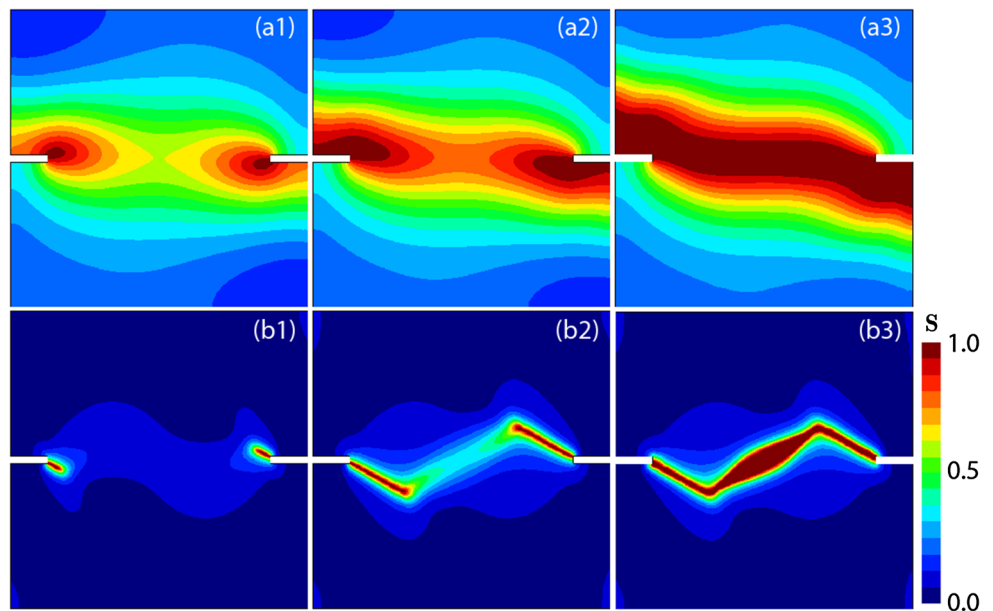


Fig. 23 Evolution of cracks for **a1** $H = 200$ mm, $\delta_n = 1.22 \times 10^{-4}$, **a2** $H = 200$ mm, $\delta_n = 1.24 \times 10^{-4}$, **a3** $H = 200$ mm, $\delta_n = 1.245 \times 10^{-4}$, **b1** $H = 2000$ mm, $\delta_n = 6.5 \times 10^{-5}$, **b2** $H = 2000$ mm, $\delta_n = 6.75 \times 10^{-5}$, and **b3** $H = 2000$ mm, $\delta_n = 7.15 \times 10^{-5}$ using the modified phase-field model

age pressure on the top surface, P_n/P_s where P_n is the average pressure on the top surface due to the imposed displacement u_n and P_s is the average pressure resulting from the lateral force, versus normalised displacement δ_n . The results from the simulation conducted by Nooru-Mohammad et al. [51] are also depicted for comparison. The maximum P_n/P_s predicted from this study is about 1.3 which is 8.33% higher than the experimental result (around 1.2). This reinforces the conclusion drawn in Sect. 6.4 that both the predicted

crack paths and the maximum force from phase-field modelling are comparable to experimental data when the utilised length scale, estimated using Eq. (41), is much smaller than the specimen size. The ratio l_0/H is a controlling factor in the accuracy of phase-field modelling. Furthermore, it also validates the performance of the proposed formula of length scale estimation in modelling mixed-mode cracks, although the formula is derived from a one-dimensional crack problem.

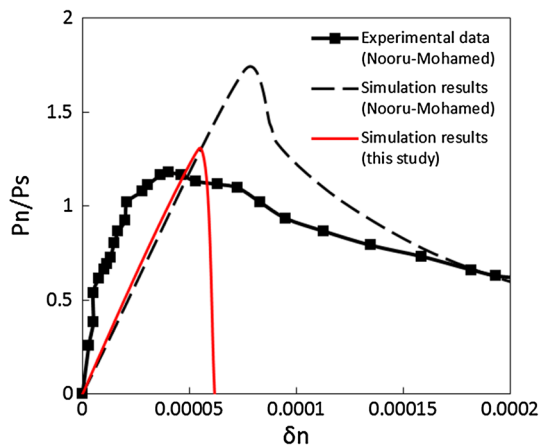


Fig. 24 Load-displacement curves for $H = 2000$ mm using the modified phase-field model

7 Conclusions and discussions

The article provides a critical numerical estimation of the accuracy of the phase-field model for brittle fracture against experimental data with particular emphasis on the length scale. The utilised phase-field model is described in detail. The length scale is regarded as a material parameter and calculated through an available formula derived from a one-dimensional crack problem. Validation simulations of a number of classical experimental tests for brittle fracture in concretes are performed using the staggered scheme with iterations. Results of both the crack paths and the load-displacement responses from the phase-field modelling are compared with available experimental data.

According to the comparison between the simulated results and experimental data, the following conclusions have been validated: (a) Regardless whether the length scale is considered a material parameter, the ratio of the length scale parameter and the specimen size has to be sufficiently small for the sake of the convergence of the regularised variational principle which is the foundation of the phase-field model. A large length scale leads to significant errors in the predicted critical force response. (b) The concerned formula for length scale estimation is derived on the assumption of a uniformly distributed crack field, whereas the tensile strength utilised is calibrated from the tensile test in which a discontinuous crack is encountered. Despite such an inconsistency, the phase-field simulations of fracture are valid when the estimated length scale is sufficiently small. The predicted crack paths are accurate and the force-displacement responses, especially the critical force response, are comparable to experimental data. (c) Despite that the formula for length scale estimation is derived from a purely tension crack, it performs well for mixed-mode brittle cracks.

(d) Strict convergence proofs of the phase-field model with energy decomposition to any variational formula for brittle fracture are not yet available; nevertheless, the model with energy decomposition produces both valid crack paths and load-displacement responses using the estimated length scale, whereas the model without energy decomposition does not even though it converges to the original variational principle.

Finally, it is noteworthy that the predicted response after the critical force does not agree well with experimental data which needs to be investigated further. Moreover, the concerned formula for length scale estimation is for the case of brittle fracture; the corresponding formulas for ductile fracture or fracture in saturated porous media can also be derived in a similar manner whose validations, however, are more complex.

Acknowledgements The authors wish to acknowledge the support of the Australian Research Council Centre of Excellence for Geotechnical Science and Engineering and the Australian Research Council Discovery Project funding scheme (Project Number DP150104257).

References

1. Griffith AA (1921) The phenomena of rupture and flow in solids. *Philos Trans R Soc Lond A Math Phys Eng Sci* 221(582–593):163–198
2. Francfort GA, Marigo JJ (1998) Revisiting brittle fracture as an energy minimization problem. *J Mech Phys Solids* 46(8):1319–1342
3. Chambolle A, Francfort GA, Marigo JJ (2009) When and how do cracks propagate? *J Mech Phys Solids* 57(9):1614–1622
4. Bourdin B, Francfort GA, Marigo JJ (2000) Numerical experiments in revisited brittle fracture. *J Mech Phys Solids* 48(4):797–826
5. Proudhon H, Li J, Wang F, Roos A, Chiaruttini V, Forest S (2016) 3D simulation of short fatigue crack propagation by finite element crystal plasticity and remeshing. *Int J Fatigue* 82(Part 2):238–246
6. Kuutti J, Kolari K (2012) A local remeshing procedure to simulate crack propagation in quasi-brittle materials. *Eng Comput* 29(2):125–143
7. Bouchard PO, Bay F, Chastel Y (2003) Numerical modelling of crack propagation: automatic remeshing and comparison of different criteria. *Comput Methods Appl Mech Eng* 192(35–36):3887–3908
8. Réthoré J, Gravouil A, Combescure A (2004) A stable numerical scheme for the finite element simulation of dynamic crack propagation with remeshing. *Comput Methods Appl Mech Eng* 193(42–44):4493–4510
9. Bouchard PO, Bay F, Chastel Y, Toveni I (2000) Crack propagation modelling using an advanced remeshing technique. *Comput Methods Appl Mech Eng* 189(3):723–742
10. Branco R, Antunes FV, Costa JD (2015) A review on 3D-FE adaptive remeshing techniques for crack growth modelling. *Eng Fract Mech* 141:170–195
11. Moës N, Belytschko T (2002) Extended finite element method for cohesive crack growth. *Eng Fract Mech* 69(7):813–833
12. Belytschko T, Gracie R, Ventura G (2009) A review of extended/generalized finite element methods for material modeling. *Model Simul Mater Sci Eng* 17(4):043001

13. Sukumar N, Moës N, Moran B, Belytschko T (2000) Extended finite element method for three-dimensional crack modelling. *Int J Numer Meth Eng* 48(11):1549–1570
14. Fries T-P, Belytschko T (2010) The extended/generalized finite element method: an overview of the method and its applications. *Int J Numer Meth Eng* 84(3):253–304
15. Abdelaziz Y, Hamouine A (2008) A survey of the extended finite element. *Comput Struct* 86(11–12):1141–1151
16. Miehe C, Welschinger F, Hofacker M (2010) Thermodynamically consistent phase-field models of fracture: variational principles and multi-field FE implementations. *Int J Numer Meth Eng* 83(10):1273–1311
17. Miehe C, Hofacker M, Welschinger F (2010) A phase field model for rate-independent crack propagation: robust algorithmic implementation based on operator splits. *Comput Methods Appl Mech Eng* 199(45–48):2765–2778
18. Schlüter A, Willenbücher A, Kuhn C, Müller R (2014) Phase field approximation of dynamic brittle fracture. *Comput Mech* 54(5):1141–1161
19. Bourdin B, Marigo J-J, Maurini C, Sicsic P (2014) Morphogenesis and propagation of complex cracks induced by thermal shocks. *Phys Rev Lett* 112(1):014301
20. Kuhn C, Müller R (2010) A continuum phase field model for fracture. *Eng Fract Mech* 77(18):3625–3634
21. Msekh MA, Sargado JM, Jamshidian M, Areias PM, Rabczuk T (2015) Abaqus implementation of phase-field model for brittle fracture. *Comput Mater Sci* 96(Part B):472–484
22. Bourdin B (2007) The variational formulation of brittle fracture: numerical implementation and extensions. In: Combescure A, Borst R, Belytschko T (eds) *IUTAM symposium on discretization methods for evolving discontinuities*. Springer Netherlands, Dordrecht
23. Liu G, Li Q, Msekh MA, Zuo Z (2016) Abaqus implementation of monolithic and staggered schemes for quasi-static and dynamic fracture phase-field model. *Comput Mater Sci* 121:35–47
24. Amor H, Marigo J-J, Maurini C (2009) Regularized formulation of the variational brittle fracture with unilateral contact: numerical experiments. *J Mech Phys Solids* 57(8):1209–1229
25. Ambati M, Gerasimov T, Lorenzis L (2014) A review on phase-field models of brittle fracture and a new fast hybrid formulation. *Comput Mech* 55(2):383–405
26. Schilling D, Borden MJ, Stolarski HK (2015) Isogeometric collocation for phase-field fracture models. *Comput Methods Appl Mech Eng* 284:583–610
27. Kuhn C, Müller R (2011) A new finite element technique for a phase field model of brittle fracture. *J Theor Appl Mech* 49(4):1115–1133
28. Borden MJ, Verhoosel CV, Scott MA, Hughes TJR, Landis CM (2012) A phase-field description of dynamic brittle fracture. *Comput Methods Appl Mech Eng* 217–220:77–95
29. Hofacker M, Miehe C (2013) A phase field model of dynamic fracture: robust field updates for the analysis of complex crack patterns. *Int J Numer Meth Eng* 93(3):276–301
30. Ambati M, Gerasimov T, De Lorenzis L (2015) Phase-field modeling of ductile fracture. *Comput Mech* 55(5):1017–1040
31. Aldakheel F, Mauthe S, Miehe C (2014) Towards phase field modeling of ductile fracture in gradient-extended elastic-plastic solids. *PAMM* 14(1):411–412
32. Ulmer H, Hofacker M, Miehe C (2013) Phase field modeling of brittle and ductile fracture. *PAMM* 13(1):533–536
33. Miehe C, Hofacker M, Schänzel LM, Aldakheel F (2015) Phase field modeling of fracture in multi-physics problems. Part II. Coupled brittle-to-ductile failure criteria and crack propagation in thermo-elastic-plastic solids. *Comput Methods Appl Mech Eng* 294:486–522
34. May S, Vignollet J, de Borst R (2015) A numerical assessment of phase-field models for brittle and cohesive fracture: Γ -Convergence and stress oscillations. *Eur J Mech A Solids* 52:72–84
35. Vignollet J, May S, Borst R, Verhoosel CV (2014) Phase-field models for brittle and cohesive fracture. *Meccanica* 49(11):2587–2601
36. Verhoosel CV, de Borst R (2013) A phase-field model for cohesive fracture. *Int J Numer Meth Eng* 96(1):43–62
37. Miehe C, Schänzel L-M (2014) Phase field modeling of fracture in rubbery polymers. Part I: finite elasticity coupled with brittle failure. *J Mech Phys Solids* 65:93–113
38. Amiri F, Millán D, Shen Y, Rabczuk T, Arroyo M (2014) Phase-field modeling of fracture in linear thin shells. *Theoret Appl Fract Mech* 69:102–109
39. Mesgarnejad A, Bourdin B, Khonsari MM (2013) A variational approach to the fracture of brittle thin films subject to out-of-plane loading. *J Mech Phys Solids* 61(11):2360–2379
40. León Baldelli AA, Bourdin B, Marigo J-J, Maurini C (2011) Fracture and debonding of a thin film on a stiff substrate: analytical and numerical solutions of a 1d variational model. Springer, Berlin
41. León Baldelli AA, Babadjian JF, Bourdin B, Henao D, Maurini C (2014) A variational model for fracture and debonding of thin films under in-plane loadings. *J Mech Phys Solids* 70:320–348
42. Mikelić A, Wheeler MF, Wick T (2015) A phase-field method for propagating fluid-filled fractures coupled to a surrounding porous medium. *Multiscale Model Simul* 13(1):367–398
43. Miehe C, Mauthe S (2016) Phase field modeling of fracture in multi-physics problems. Part III. Crack driving forces in hydro-poro-elasticity and hydraulic fracturing of fluid-saturated porous media. *Comput Methods Appl Mech Eng* 304:619–655
44. Heider Y, Markert B (2016) A phase-field modeling approach of hydraulic fracture in saturated porous media. *Mechanics Res Commun* (in press)
45. Mikelić A, Wheeler MF, Wick T (2015) Phase-field modeling of a fluid-driven fracture in a poroelastic medium. *Comput Geosci* 19(6):1171–1195
46. Nguyen TT, Yvonnet J, Bornert M, Chateau C, Sab K, Romani R, Le Roy R (2016) On the choice of parameters in the phase field method for simulating crack initiation with experimental validation. *Int J Fract* 197(2):213–226
47. Mesgarnejad A, Bourdin B, Khonsari MM (2015) Validation simulations for the variational approach to fracture. *Comput Methods Appl Mech Eng* 290:420–437
48. Kuhn C, Schlüter A, Müller R (2015) On degradation functions in phase field fracture models. *Comput Mater Sci* 108(Part B):374–384
49. Bourdin B, Francfort GA, Marigo J-J (2008) The variational approach to fracture. *J Elast* 91(1):5–148
50. Philip CP, Alberto R (1995) Size effect on fracture energy of concrete and stability issues in three-point bending fracture toughness testing. *Mater J* 92(5):483–496
51. Noor-Mohamed MB (1992) Mixed-mode fracture of concrete: an experimental approach. In: *Civil Engineering and Geosciences* (Doctoral dissertation). Delft University of Technology
52. Hamdia KM, Msekh MA, Silani M, Vu-Bac N, Zhuang X, Nguyen-Thoi T, Rabczuk T (2015) Uncertainty quantification of the fracture properties of polymeric nanocomposites based on phase field modeling. *Compos Struct* 133:1177–1190
53. Winkler BJ (2001) *Traglastuntersuchungen von unbewehrten und bewehrten Betonstrukturen auf der Grundlage eines objektiven Werkstoffgesetzes für Beton* (Doctoral dissertation). Innsbruck University, Innsbruck
54. Trunk B (1999) *Einfluss der Bauteilgröße auf die Bruchenergie von Beton* (Doctoral dissertation). Techn. Wiss. ETH Zürich